



This is a repository copy of *Biomimetic nanoporous aerogels from branched aramid nanofibers combining high heat insulation and compressive strength*.

White Rose Research Online URL for this paper:  
<https://eprints.whiterose.ac.uk/181485/>

Version: Published Version

---

**Article:**

Li, J., Li, H., Xu, L. et al. (5 more authors) (2021) Biomimetic nanoporous aerogels from branched aramid nanofibers combining high heat insulation and compressive strength. *SmartMat*, 2 (1). pp. 76-87. ISSN 2688-819X

<https://doi.org/10.1002/smm2.1019>

---

**Reuse**

This article is distributed under the terms of the Creative Commons Attribution (CC BY) licence. This licence allows you to distribute, remix, tweak, and build upon the work, even commercially, as long as you credit the authors for the original work. More information and the full terms of the licence here:  
<https://creativecommons.org/licenses/>

**Takedown**

If you consider content in White Rose Research Online to be in breach of UK law, please notify us by emailing [eprints@whiterose.ac.uk](mailto:eprints@whiterose.ac.uk) including the URL of the record and the reason for the withdrawal request.



[eprints@whiterose.ac.uk](mailto:eprints@whiterose.ac.uk)  
<https://eprints.whiterose.ac.uk/>

## RESEARCH ARTICLE

# Biomimetic nanoporous aerogels from branched aramid nanofibers combining high heat insulation and compressive strength

Jun Li<sup>1,2,3</sup> | Huaiyu Li<sup>3</sup> | Liwei Xu<sup>3</sup> | Lijun Wang<sup>3</sup> | Zhen Hu<sup>3</sup> | Li Liu<sup>3</sup> | Yudong Huang<sup>3</sup> | Nicholas A. Kotov<sup>1,2,4</sup> 

<sup>1</sup>Department of Chemical Engineering, University of Michigan, Ann Arbor, Michigan, USA

<sup>2</sup>Department of Materials Science and Engineering, University of Michigan, Ann Arbor, Michigan, USA

<sup>3</sup>Polymer Science and Engineering, Harbin Institute of Technology, Harbin, China

<sup>4</sup>Biointerfaces Institute, University of Michigan, Ann Arbor, Michigan, USA

## Correspondence

Yudong Huang, Polymer Science and Engineering, Harbin Institute of Technology, 150001 Harbin, China.  
Email: [huangyd@hit.edu.cn](mailto:huangyd@hit.edu.cn)

Nicholas A. Kotov, Department of Chemical Engineering, University of Michigan, Ann Arbor, MI 48109, USA.  
Email: [kotov@umich.edu](mailto:kotov@umich.edu)

## Funding information

Center for Hierarchical Manufacturing, National Science Foundation, Grant/Award Number: 1538180; National Natural Science Foundation of China, Grant/Award Number: 51673053

## Abstract

Materials combining efficient thermal insulation and high mechanical properties are needed in many areas of technology. Various aerogels provide a convenient design framework for thermal insulators, but they are often brittle. Furthermore, the spectrum of advanced properties is constantly expanding while requirements to the degree of control of the three-dimensional gel-forming network is constantly increasing. Here, we report on biomimetic aramid nanofibers aerogels with the structure replicating articular cartilage, prepared by supercritical drying of 3D networks held together by hydrogen bonds. Owing to the branching morphology of the nanofibers, the three-dimensional nanoscale networks with extensive percolation and high interconnectivity can be obtained. The aerogels showed high porosity with an average open pore size of 21.5 nm and correspondingly low specific density of 0.0081 g/cm<sup>3</sup>. The aerogels also possess a high compressive strength of 825 kPa at a strain of 80%. Due to the unique aramid chemistry of the parent nanofibers, aramid aerogels combine low thermal conductivity of 0.026 W/m·K with high thermal stability up to 530°C, which is unusually high for polymeric and composite materials of any type, opening a broad range of applications from electronics to space travel.

## KEYWORDS

aerogel, branched nanofiber, cartilage-like, fibril, heat resistance

## 1 | INTRODUCTION

Aerogels are known for large specific surface area, high porosity, low density, and low thermal conductivity. These properties enabled multiplicity of applications in thermal insulation,<sup>1–5</sup> optics,<sup>1,6,7</sup> acoustics,<sup>8,9</sup> and biosensing,<sup>10</sup> to name a few. Some of these applications represent iconic

marks of technological progress, such as capture and return to Earth interstellar particles.<sup>11–13</sup> In the last 5 years, there is a resurgence of aerogel research related to the emergence of aerogels from premade nanoscale components, such as carbon nanotubes,<sup>14–16</sup> graphene oxide,<sup>17–20</sup> silicon oxide,<sup>21–24</sup> boron nitride,<sup>3</sup> and cellulose.<sup>25–27</sup> While a variety of hydrogels and aerogels is increasing, so do the property

This is an open access article under the terms of the Creative Commons Attribution License, which permits use, distribution and reproduction in any medium, provided the original work is properly cited.

© 2021 The Authors. *SmartMat* published by Tianjin University and John Wiley & Sons Australia, Ltd

requirements for them. For instance, the properties set to structural thermal insulators may include high toughness, resilience to humidity, high temperature, and biological erosion. Existing hydrogels based on some nanostructures may possess these attributes while others may not. Furthermore, there is a distinct need to control and improve the interconnectivity of the three-dimensional networks producing gels. The ability of the nanoscale components to form strong junctions with one another is essential to prevent their collapse<sup>28–30</sup> into random agglomerates during both solvent exchange, supercritical drying,<sup>31,32</sup> or freeze-drying.<sup>33–35</sup> Both the need to diversify aerogel properties and to control their morphology better necessitates the development of new materials platforms for their preparation.<sup>36–38</sup>

Here, we studied the aerogels made from branched aramid nanofibers (BANFs) derived from Kevlar™ polymer, known for its high strength, stiffness, and toughness. The mechanical properties of nanofibers and, in particular, their connections with each other are essential both for prevention of network collapse under high capillary pressure (see Supporting Information) characteristic of multiple steps of aerogel preparations and for diversification of their properties. Improvements of the stiffness and the strength of the three-dimensional skeleton of the aerogel are the aerogel design strategy in this project. Importantly, it is not the mechanics of the nanoscale components that matter in this case: mechanical properties of individual nanoscale carbon components are exceptional, but those of aerogels from graphene,<sup>29,39,40</sup> graphene oxide,<sup>41,42</sup> and carbon nanotubes<sup>14,28,38,43</sup> are not. It is the combined strength of the junctions and the stiffness of the nanofibers forming the pore walls that are essential here.

Therefore, we decided to utilize BANFs<sup>38,44</sup> to reinforce the aerogel network via the facile formation of multiple junctions between the nanofibers enabled by this nanomaterial. As confirmed recently by the application of graph theory on the nanofiber networks from BANFs and collagen, they reveal percolated network structure replicating the nanofiber network of cartilage,<sup>45</sup> which is known for its exceptional mechanical properties. In addition to the high stiffness of the aramid nanofibers,<sup>46</sup> thinner segments of the branches can wrap around the thicker ones, substantially strengthening the contacts that are also taking place in many biological tissues based on nanofibers.<sup>47</sup> At the molecular scale, multiple and reconfigurable hydrogen bonds<sup>48,49</sup> at the junctions provide strong connections between BANFs replicating, in fact, nanoscale junctions known from biology.<sup>50,51</sup> The BANF aerogel obtained has a density of 0.0081 g/cm<sup>3</sup> while its specific compressive strength reaches up to 102 MPa·cm<sup>3</sup>/g, which is much higher than that of other aerogels. Additionally, the BANF-based aerogel showed large porosity, high special surface area, good thermal stability, and excellent thermal insulation.

## 2 | MATERIALS AND EXPERIMENTAL

### 2.1 | Materials

Para-aramid fibers (Kevlar 49) were purchased from E. I. Du Pont Company and used without further purification or bleaching; they were subjected to cutting and shredding processes before dissolution. The solvents used in this study, dimethyl sulfoxide (DMSO), acetonitrile, ethanol, *n*-heptane, deionized water, and other solvents, were purchased from Tianjin Fuyu Fine Chemical Co. Ltd. A supercritical CO<sub>2</sub> reactor capable of extraction was purchased from Harbin Guangming Gas Company.

### 2.2 | BANF dispersion preparation

The fabrication of aramid nanofiber aerogel (BANF aerogel) starts with the preparation of a BANF dispersion. Initially, Kevlar 49 fibers were shredded into small pieces. Subsequently, the shredded Kevlar 49 fibers (30 g) and deionized water (30 ml) were added to DMSO (3 L) and stirred vigorously for 1 day at ambient temperature, and then suitable KOH solution was added and stirred for another 6 days. After stirring and swelling, the BANF dispersion was completed.

### 2.3 | Synthesis of wet gels

The dark brown BANF dispersion was transferred to a 100-ml glass bottle and stirred for 5 min. Then various quantities of acetonitrile were slowly added to the BANF dispersion until their mass fractions of BANF dispersion in the final mixtures were 45, 50, and 55 wt%, respectively. The aerogel made from these three wet gel samples are labeled as BANF aerogel 45 wt%, BANF aerogel 50 wt%, and BANF aerogel 55 wt%, respectively. The mixtures were stirred for 5 min and transferred to 50-ml centrifuge tubes and were allowed to stand for 30 min to create the porous structure.

To improve the bonding network of BANFs, as-made wet gels were aged for 24 h.<sup>52,53</sup> After preparation, the gelation solvents were replaced with other solvents, such as DI water, *n*-heptane ethanol, and DMSO, to strengthen the BANF network. Although there was a solvent-dependent shrinkage of the BANF hydrogels (Figures S7–S9), in all cases, the aerogels obtained after supercritical drying possessed open porous structures formed by a fibrillar network (Figures 1 and S1–S3).

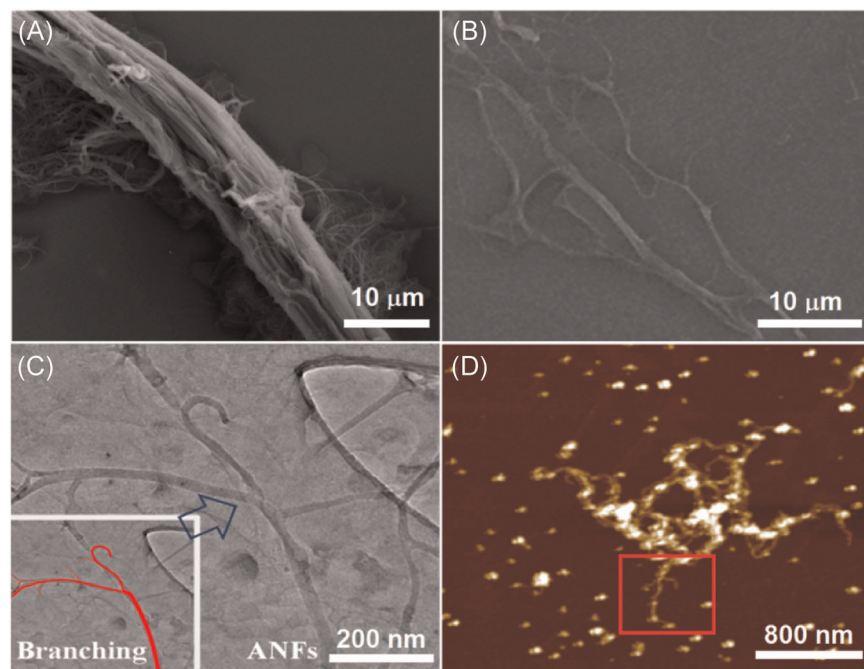


**FIGURE 1** Microscale and nanoscale morphology of branched aramid nanofibers (BANFs). (A) Scanning electron microscopy (SEM) image of the fibrils stripped from Kevlar 49 fiber. (B) SEM image of branched BANFs. (C) Transmission electron microscopy image of BANFs. The inset with the red marker highlights the fiber geometry. (D) Atomic force microscopy image of one branched BANF

## 2.4 | Synthesis of BANF aerogel

While the wet gel was standing, some stock solution precipitated from the solid phase. To facilitate the wet gel formation of stable supporting skeletons, the wet gel block was maintained in a stock solution at ambient temperature for 24 h. After aging, the wet gel block was immersed in 2-L fresh *n*-heptane to exchange the DMSO from the wet gel. Magnetic stirring was used to accelerate the extraction process. Six hours later, most of the DMSO and other solvents were removed. The removal of high surface tension of solution in wet gel block resulted in a more stable structure. Finally, the gel was dried using supercritical CO<sub>2</sub>, and the BANF aerogel monolith was investigated. The results are summarized in Figures S10–S13.

## 2.5 | Characterization

Surface and internal morphologies of the aerogels were observed by an S-4800 Field Emission Scanning Electron Microscope. All the samples were treated with spray-gold before scanning. To investigate the microstructure, samples were observed with a Tecnai G2 F30 field emission high-resolution transmission electron microscope. Furthermore, the nanoporous structures of the aerogels were studied by N<sub>2</sub> adsorption–desorption measured at 77 K using a TriStar II 3020M analyzer. The pore size distribution (PSD) and pore parameters of the aerogels were calculated by the Brunauer–Emmett–Teller (BET) method.

Chemical bonds were confirmed using an FTIR Nexus 670 spectrometer (Nicolet) in the spectral range of

600–4000 cm<sup>-1</sup>. Thermogravimetric analysis was conducted using 851e (Bruker) to study the pyrolysis temperature of the aerogels. Samples were scanned as the temperature was raised from 30°C to 1000°C at a rate of 10°C/min in a nitrogen atmosphere. The apparent densities of a series of BANF aerogels were determined by measuring the weight and regular cylinder volume. The weight of the sample was measured by an analytical balance. The diameter and height of each sample were measured multiple times by Vernier calipers. The shrinkage of each aerogel block was measured according to Equation (1), where  $V_1$  and  $V_2$  were the volumes of aramid nanofibers gel and BANF aerogel, respectively. The volume of each sample before and after drying was measured multiple times using Vernier calipers.

The porosity of each sample was calculated using the apparent density of BANF aerogel and the skeleton density of BANF aerogel according to Equation (2)<sup>54,55</sup> where  $\rho_b$  was the apparent density of BANFs, and  $\rho_s$  was fixed at 1.44 g/cm<sup>3</sup>, based on the product data provided by DuPont Company. The stress–strain curves of BANF aerogels were measured by an Istron-5569 electronic universal testing instrument when all the samples were cut into the same cylinder blocks ( $\Phi 8 \times 16$  mm).

$$\text{Shrinkage (\%)} = (V_1 - V_2) / V_1, \quad (1)$$

$$\text{Porosity (\%)} = (1 - \rho_b / \rho_s) \times 100. \quad (2)$$

The plating method was used to determine the thermal conductivity of samples ( $\Phi 18 \times 3$  mm). First, the relative humidity was controlled to be between 45% and 55%. Then, each sample was sandwiched between

two glass plates (reference materials) of 3-mm thickness. The sandwich was placed between a heat source (heated copper sheet) and a cold source (ice water mixture in a glass box). The temperature of the heat source remained constant at 120°C, and the cold source was maintained at 0°C. The warm current introduced a range of temperature gradients across the sandwich, and temperature mapping was obtained through emissivity. As the thermal conductivity of the reference material glass is known, the heat flux in the sandwich could be calculated. The thermal conductivity of BANF aerogel could also be calculated utilizing the Fourier equation. The fitted linear regression lines of heat flux and temperature gradient suggest a negligible contribution of convection side losses during the measurements.

### 3 | RESULTS AND DISCUSSION

It was previously found that 1-wt% aramid nanofiber hydrogels<sup>56,57</sup> showed a much higher shear modulus than 1-wt% hydrogel made from other nanofibers and rod-like nanoscale materials,<sup>58–60</sup> which indicates that these BANFs have substantially better three-dimensional connectivity and stronger fiber-to-fiber contacts than other hydrogels.<sup>41,42,58</sup> The drastic change of dynamic mechanical properties was associated with unique branched geometry that was confirmed in the later studies.<sup>61–63</sup> None of the other

artificial nanoscale materials have similar fractal geometry at that time, opening a possibility to understand the fundamental significance and utility of such nanoscale dispersions.

Aerogels can be considered to be a solid made from nanoscale trusses. As an increase in contact points prevents slipping or breaking of the trussed structures, the branched morphology of the components is expected to benefit its resistance to external and internal pressure<sup>10,35,38,41,64,65</sup> because an increase in the number of contact points prevents slipping or breaking of the trussed structures.<sup>66–68</sup> Amphiphilic nature of BANFs also helps to increase the attraction between the fibers to strengthen the junction—the weakest parts of aerogel networks. In this perspective, BANF and other gels also replicate the organization of nanofiber-based biological tissues.

Therefore, we used BANFs instead of straight nanofibers to produce aerogel expecting to see a substantial increase in mechanical properties and potentially a decrease in pore size. Briefly, BANFs were made by controlled solvolysis of macroscale Kevlar 49 fibers via abstraction of protons from aramid chains by KOH. The dissociation of intermolecular bonds leads to splitting into nanofibers. Depending on the solvolysis conditions, the obtained nanofibers acquire a branched structure (Figure 2 and Schematics S1). Such morphology is likely to reflect their structural organization in the macroscale precursor.<sup>69</sup>

The surface of BANF contains many polar groups, such as  $-\text{COOH}$ ,  $-\text{NH}-$ , and  $-\text{NH}_2$ .<sup>33</sup> The negative charges on the BANF surface in basic media (Figure S1) provide them

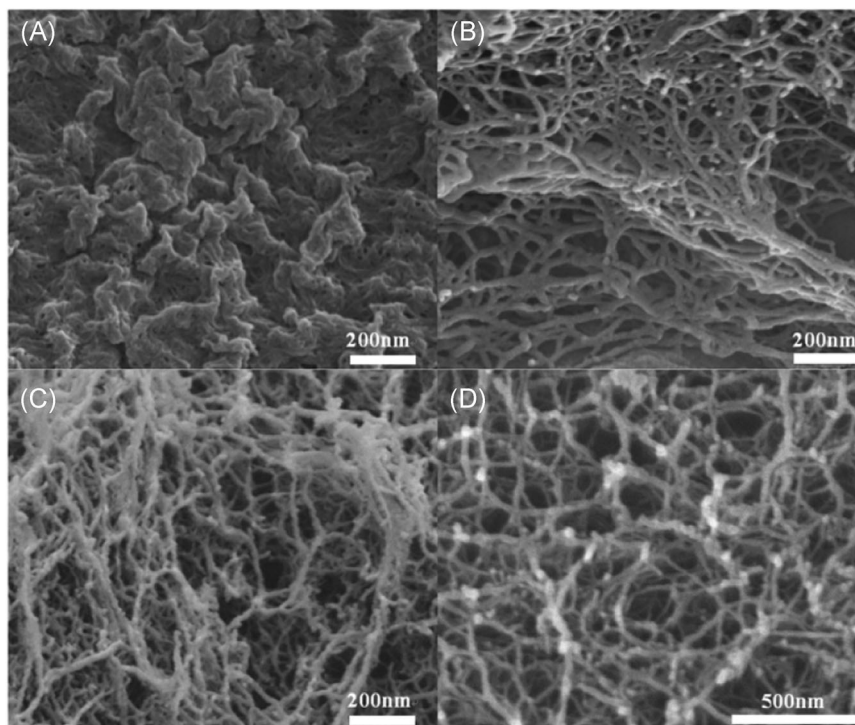


**FIGURE 2** Scanning electron microscopy images of branched aramid nanofiber aerogels showing the effects of different exchange solvents: (A) deionized water, (B) no exchange solvent, (C) ethanol, and (D) *n*-heptane

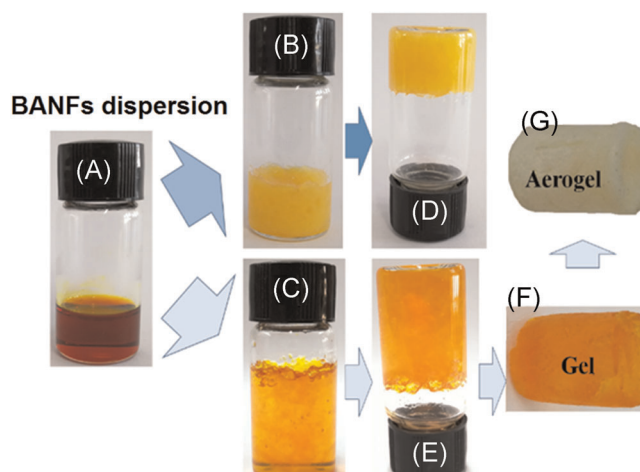


**FIGURE 3** Synthetic steps for preparation of branched aramid nanofiber (BANF) gels. (A) BANFs dispersion in dimethyl sulfoxide (DMSO). (B,C) BANF gel made by using solvent exchange with water (B) and acetonitrile (C). (D,E) Demonstration of the gelation of (B,C) by turning the flask upside down. (F) Self-standing BANF gel. (G) BANF aerogel. It can be seen that the volume swelling of gelatin obtained by gelation of acetonitrile is much larger than that of the gel obtained by water gel, indicating that the nanofibers in the samples obtained by gelation of acetonitrile are more stretched

dispersion, as well as excellent colloidal stability.<sup>56,70</sup> Furthermore, the presence of  $-\text{COOH}$  and  $-\text{NH}_2$  groups enables the formation of interfiber hydrogen bonds<sup>38,56</sup> and potentially the peptide bonds.

The association of nanofibers with each other can be promoted by solvent exchange. We tried several types of solvents to induce the phase change from BANFs dispersion into a gel and aerogel (Tables S1 and S2). The volume of obtained BANF hydrogels decreased compared with the initial BANFs dispersion (Table S3). The obtained aerogel showed a different structure, as shown in Figure 3. Meanwhile, the gelation process is accompanied by color change; using acetonitrile, the solution color changed from red to light orange, and for the other solvents, the color changed from red to light yellow (Figure 1). However, no BANF gel was formed for *N,N*-dimethylformamide under a variety of conditions because of its weak protonation. Conversely, the gradual gelation of BANFs caused by the addition of acetonitrile takes about 5 min to complete.<sup>71</sup> The volume of hydrogel does not change significantly after the gelation point.

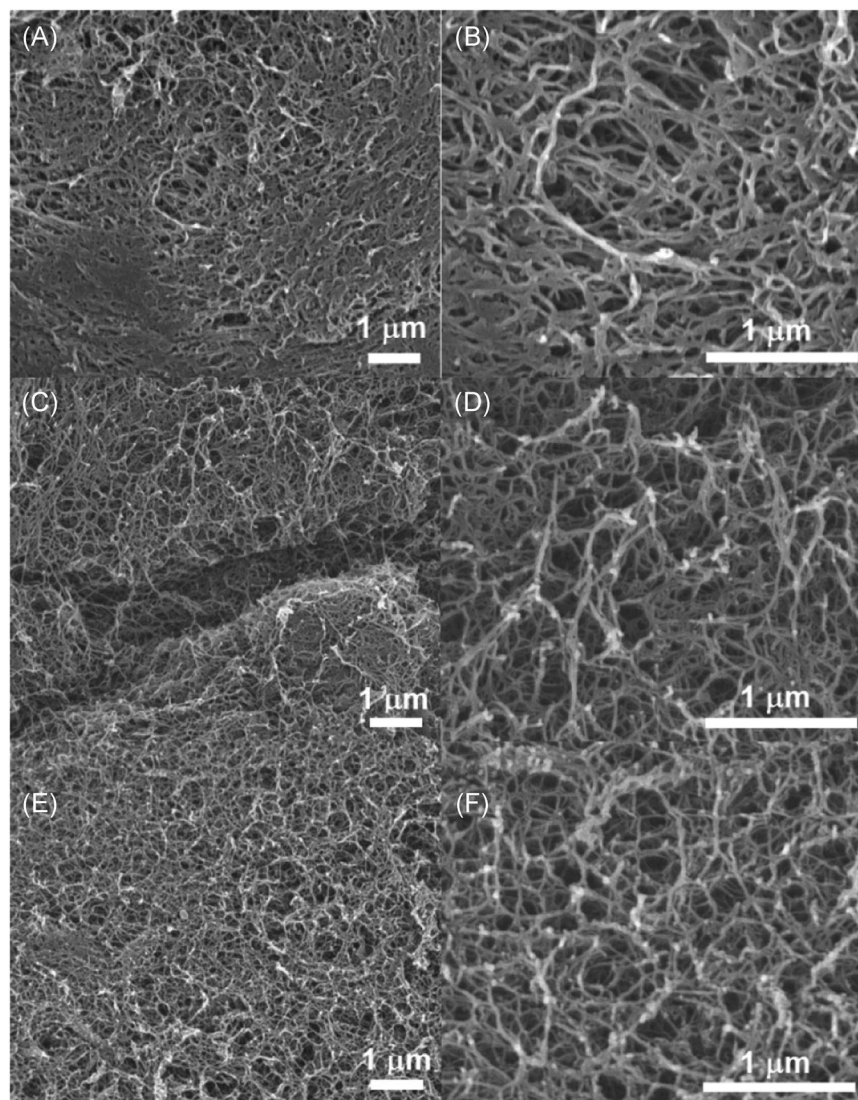
The presence of hydrogen bonds between BANFs was confirmed by the  $3450\text{ cm}^{-1}$  peak in the FTIR spectra (Figure S2). We concluded that acetonitrile is the best reagent for controlling the gelation process of BANFs dispersion due to its greater overall volume of the gel than for other solvents, which, in turn, means high porosity desirable in aerogels.<sup>72,73</sup>

BANFs dispersion concentration also affected the structure of different aerogels. As the concentration of BANFs dispersion increases, the porous structure forms more homogeneously (Figure 4), and the apparent density

of the aerogel decreases (Figure 5A). Similarly, shrinkage of aerogel from the gel decreases with increasing BANFs dispersion concentration (Figure 5B), which is associated with an increase in stiffness of the framework created by BANF that resists capillary forces during drying.<sup>74</sup> Most of the pores in the BANF aerogel were maintained through the solvent exchange and drying processes when the concentration of BANFs dispersion increases from 40 to 55 wt% (Figure 5C). However, when the concentration increases to more than 55 wt%, the porosity decreases because of the increasing aggregation of BANFs. The aerogel made from the BANFs dispersion of 55 wt% has the lowest density of  $0.0081\text{ g/cm}^3$ , which is comparable or even lower than other reported aerogels (Figure 5D).<sup>75,76</sup> The porosity of 55 wt% BANF aerogel was 99.4%, and the network was also more regular and had fewer breaks than the other two.

To investigate the microstructure and contact point interactions of our BANF aerogel, the differences between BANF aerogel and Kevlar 49 were contrasted in their FTIR spectra. FTIR spectra of the dry BANF aerogels (Figure S3) show a broad and strong peak at  $3321\text{ cm}^{-1}$ , which is attributed to the N–H stretching vibrations. A peak observed at  $1645\text{ cm}^{-1}$  is associated with C=O stretching vibrations. The peak at  $1545\text{ cm}^{-1}$  is ascribed to N–H deformation and C–N stretching-coupled modes. The peak at approximately  $1516\text{ cm}^{-1}$  represents C=C stretching vibrations of an aromatic ring. The stretching vibration of the  $\text{C}_6\text{H}_5\text{-N}$  bond (Ph-N) emerges at  $1322\text{ cm}^{-1}$ . The peak at  $1021\text{ cm}^{-1}$  corresponds to the in-plane stretching vibration of C–H bonds.<sup>57</sup> One can see that N–H and C=O stretching vibrations of BANF aerogel have stronger peaks

**FIGURE 4** Scanning electron microscopy images at low (left) and high (right) magnification of branched aramid nanofiber (BANF) aerogels made using different concentrations of BANFs. (A,B) BANF aerogel 45 wt%. (C,D) BANF aerogel 50 wt%. (E,F) BANF aerogel 55 wt%. According to (B, D, and F) the joints of BANFs aerogels become thinner at the same magnification. This further proves that the porosity of BANF aerogels becomes larger as the concentrations of BANFs increases



compared with those of Kevlar 49, attributed to stronger hydrogen bonds in BANF aerogel. This observation demonstrates the entanglement of nanofibers in BANF aerogels.<sup>38</sup>

Compared with many other aerogels, those from BANF display high thermal stability inherited from Kevlar 49 fiber (Figure S4). A weight loss of 2% occurs before 530°C, which could be attributed to thermal decomposition of the terminal groups, such as the carboxyl and amino groups.<sup>38,77</sup> The main decomposition temperature of BANF aerogel is 553°C. Kevlar 49 fiber represents a higher degradation temperature and carbonization rate, which indicates decreased compactness and increased specific surface damage to thermal stability.

Nitrogen sorption measurements were conducted to further examine the pore structure of various BANF aerogels. Figures 6A and 6B show the N<sub>2</sub> adsorption–desorption isotherms and the pore-size distribution curves of different BANF aerogels, respectively. These isotherms are classified

as Type IV with hysteresis loops, closely related to the occurrence of capillary condensation,<sup>78,79</sup> indicating mesoporosity. The surface areas were calculated using BET analysis, and the BET-specific surface areas were found to range from 396 to 542 m<sup>2</sup>/g (Figure S5), which are larger than those of branched BANF aerogels gelled with water.<sup>38</sup> The PSDs were analyzed by the Barret–Joyner–Harrenda method, and the wide PSDs ranged from 2 to 70 nm. The average pore size ranged from 10.8 to 21.5 nm, depending on the concentration of BANFs.

The total thermal conductivity can be represented as the sum of contributions from three parts: heat transfer through solid, heat transfer through gas, and heat radiation.<sup>80</sup> For the BANF aerogel, heat transfer through gas mainly consists of two parts: conduction through the gas itself and convection of gas. The averaged pore sizes in BANF aerogels ranged from 10.8 to 21.5 nm. These values are lower than the mean free path of the N<sub>2</sub> and O<sub>2</sub> molecules (~70 nm),<sup>80,81</sup> which must result in low thermal conductivity. Indeed, the thermal

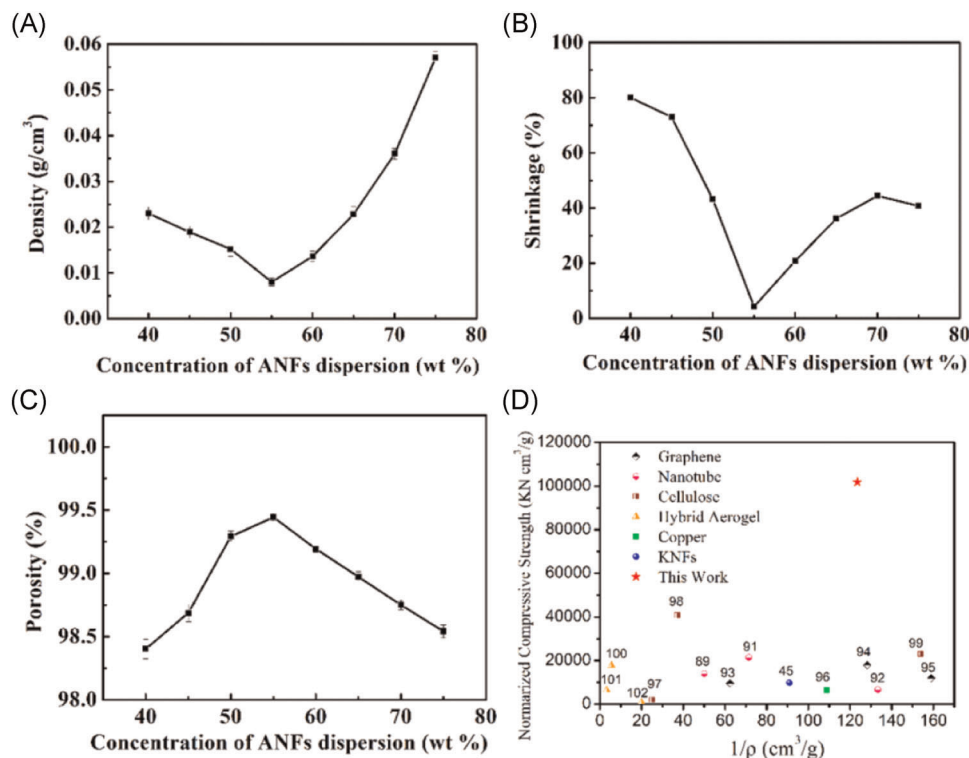


FIGURE 5 (A) Relationship between the concentration of branched aramid nanofibers (BANFs) and density. (B) Relationship between concentration of BANFs and shrinkage. (C) Relationship between concentration of BANFs and porosity. (D) Comparison of our BANF aerogel with other aerogels reported in the literature

conductivity of 0.026 W/m·K (Figure 7) of BANF aerogels approaches the thermal conductivity of air at room temperature, 0.023 W/m·K. This value is also lower than that for Kevlar 49 fiber 0.045 W/m·K and the values reported before for aramid aerogels without controlled branching was 0.028 W/m·K, as reported in Leventis et al.<sup>76</sup> As expected, the thermal conductivity was found to decrease as BANFs dispersion concentration increases (Figure 7D). We tested the thermal insulation properties of aerogel materials, as shown in Figure 7E–G. After 5 min of baking with a lighter flame, there is no change in orchid on the top of BANF aerogel, which indicates that the aerogel insulation is

excellent. From the side of aerogels, carbonization can be seen in the baking mask, and the carbonization layer is very thin, indicating that the transmission of high temperature is limited under the barrier of aerogels.

Branching also affects the shear stress–strain curve of BANF aerogel (Figure 8 and Table S4). Ultimate strength at 80% strain shows a linear elastic deformation region ending at the strain of 2%, followed by a softening region where plastic deformation begins to occur.<sup>82</sup> After being compressed to 80% of its original length, the aerogel shows favorable toughness, without any cracks. The compressive energy could be absorbed by the strong

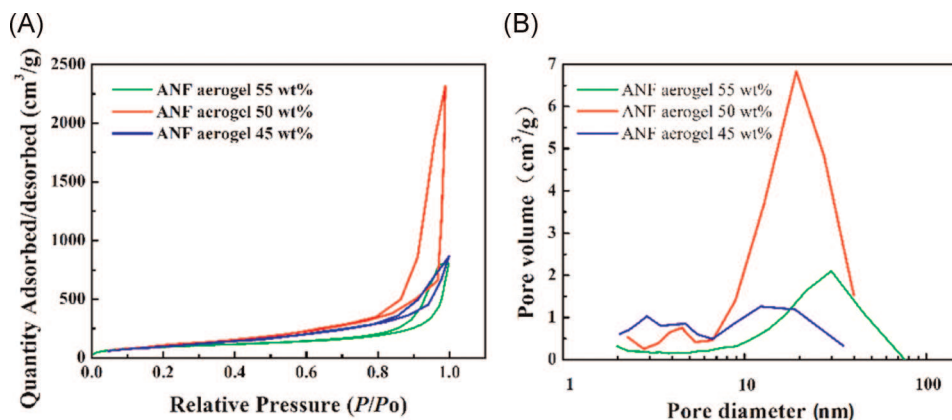
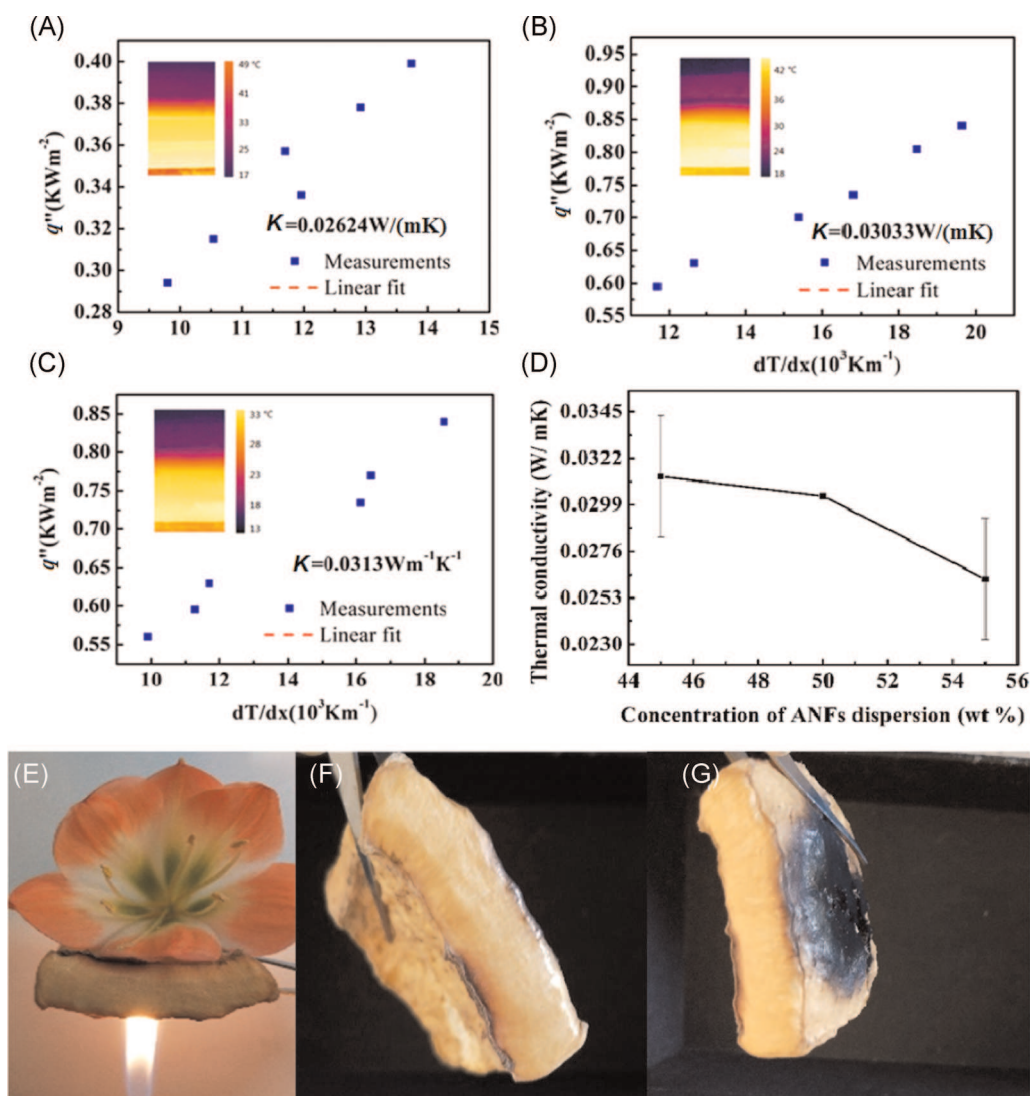


FIGURE 6 (A) Nitrogen adsorption/desorption curves of branched aramid nanofiber (BANF) aerogels. (B) Pore distributions of BANF aerogels





**FIGURE 7** Thermal conductivity of branched aramid nanofiber (BANF) aerogels. The insets in each plot are the images obtained by an infrared (IR) microscope. (A) Thermal conductivity of BANF aerogel 55 wt%. (B) Thermal conductivity of BANF aerogel 50 wt%. (C) Thermal conductivity of BANF aerogel 45 wt%. (D) Relationship between concentration of BANFs and BET thermal conductivity in which the  $q''$  of the Y axis in (A), (B), and (C) mean the heat flux density. The thermal conductivity decreases with BANFs dispersion concentration because the network formed in BANF aerogel 55 wt% is more regular and has fewer breaks than the other two. (E) BANF aerogel was baked with lighter flame for 5 min, with the orchid being laid on top of it, which indicates that the aerogel insulation is excellent. (F, G) Side view of aerogel. Carbonization can be seen in the baking edge. The carbonization layer is very thin, indicating that the transmission of high temperature is limited under the barrier of aerogels

three-dimensional network interconnection and contact points of nanofibers, leading to elastic deformation.<sup>83</sup> The compressive strength of BANF aerogel reached 825 kPa at a compressive strain of 80%, which is about five times greater than the values measured for graphene-, carbon nanotube-, and cellulose-based aerogels.<sup>84–87</sup> Compressive strength normalized by the density is 102 MPa/cm<sup>3</sup>·g for BANF aerogels, which is also much larger than that of other aerogels; even the strongest hybrid aerogels reported the state-of-the-art in the field<sup>29,38,86,88–100</sup> (Figure 5D) while demonstrating

excellent flexibility (Figure S6). These combinations of mechanical properties can also be attributed to the cartilage-like percolated network structure.

The finite element model of BANF gel in Figure 8D,E helps to simulate the mechanical deformations of aramid nanofiber gel during deformations. For BANF nanofibers forming the pore walls, elastic modulus of 126 GPa, density of 1.44 g/cm<sup>3</sup>, and Poisson ratio of 0.42 were used in simulations. One can clearly see that under pressure, stress is concentrated on the junction points, which confirmed our aerogel design strategy. When the

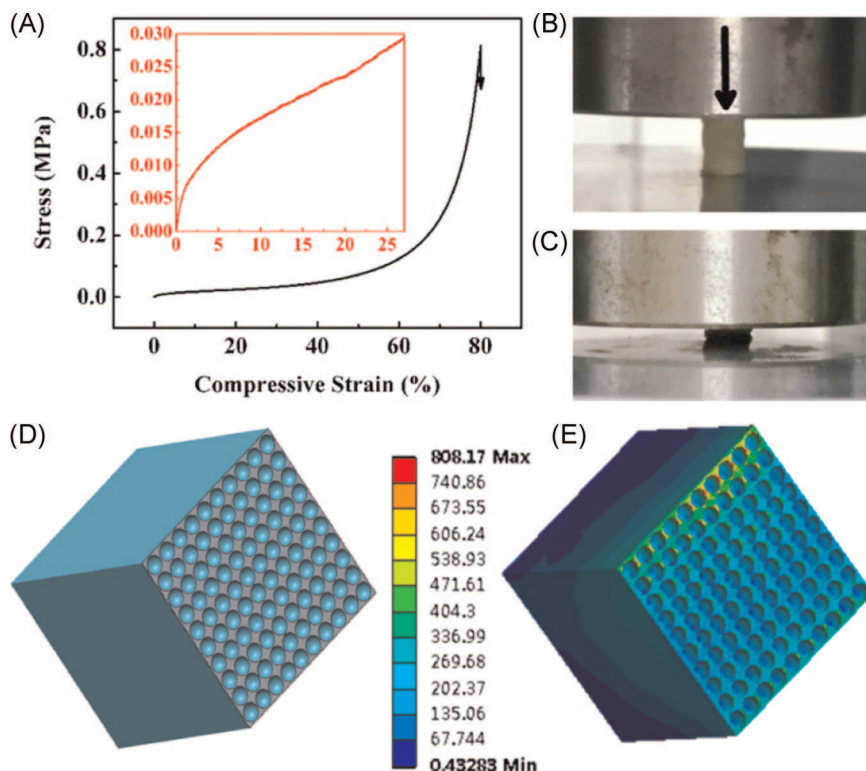


**FIGURE 8** The branched aramid nanofiber (BANF) sample under pressure. (A) Representative compression data of BANF aerogels (diameter = 0.8 cm, length:diameter ratio = 2:1). Inset: strain region (<30%) magnified. The photo of compressed BANF aerogels sample at a strain of (B) 0% and (C) 80%. (D) The cheese structure of microporous BANF aerogels. (E) The stress distribution simulation in the microporous BANF aerogels under pressure

pressure is 50 MPa, the mass stress concentration is 808 MPa, providing the numerical reference point for further development of these materials.

## 4 | CONCLUSIONS


The BANF dispersions form a uniform three-dimensional open network via gelation with acetonitrile. The primary solvent-rich gel can be converted into an aerogel by media exchange with *n*-heptane, followed by supercritical CO<sub>2</sub> drying. The resulting biomimetic material exhibits low density and high porosity, which yields outstanding thermal insulation. The entanglement of individual nanofibers and the high strength of the parent polymer results in a fibrous network with remarkable mechanical properties that stand out among the properties of known composite, polymeric, or inorganic aerogels. The unique combination of properties endows cartilage-like BANF aerogels with multiple potential applications from thermal insulation for processors in computers to the structural elements in spacecrafts, which is further augmented by the simplicity of their production, including the recycling of used aramid fabrics.

## ACKNOWLEDGMENTS

We thank the National Natural Science Foundation of China (No. 51673053) and the Natural Science Foundation of Heilongjiang Province (No. LC2017024). This study was also partially funded by the National Science Foundation (NSF)

projects #1463474 “Energy- and Cost-Efficient Manufacturing Employing Nanoparticles” and #1538180 “Layered Composites from Branched Nanofibers for Lithium Ion Batteries.”

## ORCID

Nicholas A. Kotov  <https://orcid.org/0000-0002-6864-5804>

## REFERENCES

- Günay AA, Kim H, Nagarajan N, et al. Optically transparent thermally insulating silica aerogels for solar thermal insulation. *ACS Appl Mater Interfaces*. 2018;15:12603-12611.
- Li T, Song J, Zhao X, et al. Anisotropic, lightweight, strong, and super thermally insulating nanowood with naturally aligned nanocellulose. *Sci Adv*. 2018;3:eaar3724.
- Xu X, Zhang Q, Hao M, et al. Double-negative-index ceramic aerogels for thermal superinsulation. *Science*. 2019;6428:723-727.
- Hopkins PE, Kaehr B, Piekos ES, Dunphy D, Brinker CJ. Minimum thermal conductivity considerations in aerogel thin films. *J Appl Phys*. 2012;111:113532.
- Baker CH, Jordan DA, Norris PM. Application of the wavelet transform to nanoscale thermal transport. *Phys Rev B* 2012;10:104306.
- Wang P, Körner W, Emmerling A, Beck A, Kuhn J, Fricke J. Optical investigations of silica aerogels. *J Non Cryst Solids*. 1992;145:141-145.
- Xiao L, Grogan MDW, Wadsworth WJ, England R, Birks TA. Stable low-loss optical nanofibres embedded in hydrophobic aerogel. *Opt Express*. 2011;2:764-769.

8. Gibiat V, Lefevre O, Woignier T, Pelous J, Phalippou J. Acoustic properties and potential applications of silica aerogels. *J Non Cryst Solids*. 1995;186:244-255.
9. Hrubesh LW. Aerogel applications. *J Non Cryst Solids*. 1998; 1-3:335-342.
10. Ma Y, Yue Y, Zhang H, et al. 3D synergistical MXene/reduced graphene oxide aerogel for a piezoresistive sensor. *ACS Nano*. 2018;4:3209-3216.
11. Sandford SA, Aleon J, Alexander CMO, et al. Organics captured from comet 81P/wild 2 by the stardust spacecraft. *Science*. 2006;5806:1720-1724.
12. McKeegan KD, Aleon J, Bradley J, et al. Isotopic compositions of cometary matter returned by stardust. *Science*. 2006; 5806:1724-1728.
13. Tsou P, Brownlee DE, Sandford SA, Hörz F, Zolensky ME. Wild 2 and interstellar sample collection and Earth return. *J Geophys Res Planets*. 2003;108(10):123-125.
14. Kuznetsov AA, Fonseca AF, Aliev AE, et al. Giant-stroke, superelastic carbon nanotube aerogel muscles. *Science*. 2009; 323(5921):1575-1578.
15. Hamed MM, Hajian A, Fall AB, et al. Highly conducting, strong nanocomposites based on nanocellulose-assisted aqueous dispersions of single-wall carbon nanotubes. *ACS Nano*. 2014; 8(3):2467-2476. <https://doi.org/10.1021/nn4060368>
16. Zhai L, Seal S, Joung D, et al. Ultralight multiwalled carbon nanotube aerogel. *ACS Nano*. 2010;4(12):7293-7302. <https://doi.org/10.1021/nn102246a>
17. Xu X, Li H, Zhang Q, et al. Self-sensing, ultralight, and conductive 3D graphene/iron oxide aerogel elastomer deformable in a magnetic field. *ACS Nano*. 2015;9(4):3969-3977. <https://doi.org/10.1021/nn507426u>
18. Kashani H, Ito Y, Han J, Liu P, Chen M. Extraordinary tensile strength and ductility of scalable nanoporous graphene. *Sci Adv*. 2019;5(2):eaat6951. <https://doi.org/10.1126/sciadv.aat6951>
19. Yang H, Li Z, Lu B, et al. Reconstruction of inherent graphene oxide liquid crystals for large-scale fabrication of structure-intact graphene aerogel bulk toward practical applications. *ACS Nano*. 2018;12(11):11407-11416. <https://doi.org/10.1021/acsnano.8b06380>
20. Wang C, Chen X, Wang B, et al. Freeze-casting produces a graphene oxide aerogel with a radial and centrosymmetric structure. *ACS Nano*. 2018;12(6):5816-5825. <https://doi.org/10.1021/acsnano.8b01747>
21. Soleimani Dorcheh A, Abbasi MH. Silica aerogel: synthesis, properties and characterization. *J Mater Process Technol*. 2008; 199(1):10-26. <https://doi.org/10.1016/j.jmatprotec.2007.10.060>
22. Tai Y, Watanabe M, Kaneko K, et al. Preparation of gold cluster/silica nanocomposite aerogel via spontaneous wet-gel formation. *Adv Mater*. 2001;13:1611-1614.
23. Su L, Wang H, Niu M, et al. Ultralight, recoverable, and high-temperature-resistant sic nanowire aerogel. *ACS Nano*. 2018; 12(4):3103-3111. <https://doi.org/10.1021/acsnano.7b08577>
24. Zu G, Shimizu T, Kanamori K, et al. Transparent, superflexible doubly cross-linked polyvinylpolymethylsiloxane aerogel superinsulators via ambient pressure drying. *ACS Nano*. 2018;12(1): 521-532. <https://doi.org/10.1021/acsnano.7b07117>
25. Liu H, Geng B, Chen Y, Wang H. Review on the aerogel-type oil sorbents derived from nanocellulose. *ACS Sustain Chem Eng*. 2017;5(1):49-66. <https://doi.org/10.1021/acssuschemeng.6b02301>
26. Song J, Chen C, Yang Z, et al. Highly compressible, anisotropic aerogel with aligned cellulose nanofibers. *ACS Nano*. 2018;12(1):140-147. <https://doi.org/10.1021/acsnano.7b04246>
27. Yeo SJ, Oh MJ, Yoo PJ. Structurally controlled cellular architectures for high-performance ultra-lightweight materials. *Adv Mater*. 2018;1803670:1-26. <https://doi.org/10.1002/adma.201803670>
28. Yang C, Liu N, Zeng W, et al. Superelastic and ultralight electron source from modifying 3D reduced graphene aerogel microstructure. *Nano Energy*. 2017;33:280-287. <https://doi.org/10.1016/j.nanoen.2017.01.019>
29. Zhao X, Yao W, Gao W, Chen H, Gao C. Wet-spun superelastic graphene aerogel millispheres with group effect. *Adv Mater*. 2017;29(35):1-9. <https://doi.org/10.1002/adma.201701482>
30. Tan C, Fung BM, Newman JK, Vu C. Organic aerogels with very high impact strength. *Adv Mater*. 2001;13(9):644-646.
31. Zhang X, Sui Z, Xu B, et al. Mechanically strong and highly conductive graphene aerogel and its use as electrodes for electrochemical power sources. *J Mater Chem*. 2011;21(18): 6494. <https://doi.org/10.1039/c1jm10239g>
32. Rudaz C, Courson R, Bonnet L, Calas-Etienne S, Sallée H, Budtova T. Aeropectin: fully biomass-based mechanically strong and thermal superinsulating aerogel. *Biomacromolecules*. 2014;15(6):2188-2195. <https://doi.org/10.1021/bm500345u>
33. Li WC, Lu AH, Guo SC. Characterization of the microstructures of organic and carbon aerogels based upon mixed cresol-formaldehyde. *Carbon*. 2001;39(13):1989-1994. [https://doi.org/10.1016/S0008-6223\(01\)00029-X](https://doi.org/10.1016/S0008-6223(01)00029-X)
34. Whitaker S. A theory of drying in porous media. *Adv. Heat Transf*. 1977:119-203.
35. Chen W, Yu H, Li Q, Liu Y, Li J. Ultralight and highly flexible aerogels with long cellulose I nanofibers. *Soft Matter*. 2011;7(21):10360-10368. <https://doi.org/10.1039/c1sm06179h>
36. Bi H, Huang X, Wu X, et al. Carbon microbelt aerogel prepared by waste paper: an efficient and recyclable sorbent for oils and organic solvents. *Small*. 2014;10(17):3544-3550. <https://doi.org/10.1002/sml.201303413>
37. Yang M, Cao K, Yeom B, et al. Aramid nanofiber-reinforced transparent nanocomposites. *J Compos Mater*. 2015;49: 1873-1879. <https://doi.org/10.1177/0021998315579230>
38. Zhu J, Yang M, Emre A, et al. Branched aramid nanofibers. *Angew Chemie Int Ed*. 2017;56(39):11744-11748. <https://doi.org/10.1002/anie.201703766>
39. Kotal M, Kim H, Roy S, Oh IK. Sulfur and nitrogen co-doped holey graphene aerogel for structurally resilient solid-state supercapacitors under high compressions. *J Mater Chem A*. 2017;5(33):17253-17266. <https://doi.org/10.1039/c7ta05237e>
40. Nguyen ST, Feng J, Ng SK, Wong JPW, Tan VBC, Duong HM. Advanced thermal insulation and absorption properties of recycled cellulose aerogels. *Colloids Surf A Physicochem Eng Asp*. 2014;445:128-134. <https://doi.org/10.1016/j.colsurfa.2014.01.015>
41. Lei Y, Hu Z, Cao B, Chen X, Song H. Enhancements of thermal insulation and mechanical property of silica aerogel monoliths by mixing graphene oxide. *Mater Chem Phys*. 2017;187:183-190. <https://doi.org/10.1016/j.matchemphys.2016.11.064>
42. Mi X, Huang G, Xie W, Wang W, Liu Y, Gao J. Preparation of graphene oxide aerogel and its adsorption for Cu<sup>2+</sup> ions. *Carbon*. 2012;50(13):4856-4864. <https://doi.org/10.1016/j.carbon.2012.06.013>

43. Kim KH, Vural M, Islam MF. Single-walled carbon nanotube aerogel-based elastic conductors. *Adv Mater.* 2011;23(25):2865-2869. <https://doi.org/10.1002/adma.201100310>
44. Wang M, Emre A, Tung SO, et al. Biomimetic solid-state Zn<sup>2+</sup> electrolyte for corrugated structural batteries. *ACS Nano.* 2019;13(2):1107-1115. <https://doi.org/10.1021/acsnano.8b05068>
45. Kotov NA, Zhang H, Vecchio D, et al. Graph theoretical design of biomimetic aramid nanofiber nanocomposites as insulation coatings for implantable bioelectronics. *bioRxiv.* 2020. <https://doi.org/10.1101/2020.12.28.424604>
46. O'Connor I, Hayden H, Coleman JN, Gun'ko YK. High-strength, high-toughness composite fibers by swelling kevlar in nanotube suspensions. *Small.* 2009;5(4):466-469. <https://doi.org/10.1002/smll.200801102>
47. Pallela SR, Andres C, Chen W, Xu C, Wang L, Kotov NA. Permselectivity replication of artificial glomerular basement membranes in nanoporous collagen multilayers. *J Phys Chem Lett.* 2011;2(16):2067-2072. <https://doi.org/10.1021/jz200880c>
48. Dewapriya MAN, Rajapakse RKND, Nigam N. Influence of hydrogen functionalization on the fracture strength of graphene and the interfacial properties of graphene-polymer nanocomposite. *Carbon.* 2015;93:830-842. <https://doi.org/10.1016/j.carbon.2015.05.101>
49. Han Z, Tang Z, Li P, Yang G, Zheng Q, Yang J. Ammonia solution strengthened three-dimensional macro-porous graphene aerogel. *Nanoscale.* 2013;5(12):5462-5467. <https://doi.org/10.1039/c3nr00971h>
50. Rustom A, Saffrich R, Markovic I, Walther P, Gerdes H. Nanotubular highways for intercellular organelle transport. *Science.* 2004;303:1007-1010.
51. Dimaio J, Ruthel G, Cannon JJ, Malfara MF, Povelones ML. The single mitochondrion of the kinetoplastid parasite *Criethidia fasciculata* is a dynamic network. *PLOS One.* 2018;13:e0202711.
52. Liu M, Zhou D, He YB, et al. Novel gel polymer electrolyte for high-performance lithium-sulfur batteries. *Nano Energy.* 2016;22:278-289. <https://doi.org/10.1016/j.nanoen.2016.02.008>
53. Andrades RC, Munhoz AH Jr, de Miranda LF. Gamma-alumina synthesis from ceramic powders of pseudoboehmite obtained by the sol-gel process. *Mater Sci Forum.* 2016;881:12-17. <https://doi.org/10.4028/www.scientific.net/msf.881.12>
54. Hegde ND, Rao AV. Effect of processing temperature on gelation and physical properties of low density TEOS based silica aerogels. *J Sol-Gel Sci Technol.* 2006;38(1):55-61. <https://doi.org/10.1007/s10971-006-5348-z>
55. Hu H, Zhao Z, Wan W, Gogotsi Y, Qiu J. Ultralight and highly compressible graphene aerogels. *Adv Mater.* 2013;25(15):2219-2223. <https://doi.org/10.1002/adma.201204530>
56. Yang M, Cao K, Sui L, Qi Y, Zhu J, Waas A. Dispersions of aramid nanofibers: a new piece of nanoscale toolset. *ACS Nano.* 2011;5(9):6945-6954.
57. Cao K, Siepermann CP, Yang M, et al. Reactive aramid nanostructures as high-performance polymeric building blocks for advanced composites. *Adv Funct Mater.* 2013;23(16):2072-2080. <https://doi.org/10.1002/adfm.201202466>
58. Wu X, Moon RJ, Martini A. Crystalline cellulose elastic modulus predicted by atomistic models of uniform deformation and nanoscale indentation. *Cellulose.* 2013;20(1):43-55. <https://doi.org/10.1007/s10570-012-9823-0>
59. Robinson JT, Zalalutdinov M, Baldwin JW, Snow ES. Wafer-scale reduced graphene oxide films for nanomechanical devices. *Nano Lett.* 2008;8(08):3441-3445.
60. Rey-Raap N, Calvo EG, Menéndez JA, Arenillas A. Exploring the potential of resorcinol-formaldehyde xerogels as thermal insulators. *Microporous Mesoporous Mater.* 2017;244:50-54. <https://doi.org/10.1016/j.micromeso.2017.02.044>
61. Ford CM, Gibson LJ. Uniaxial strength asymmetry in cellular materials: an analytical model. *Int J Mech Sci.* 1998;40(6):521-531. [https://doi.org/10.1016/s0020-7403\(97\)00064-7](https://doi.org/10.1016/s0020-7403(97)00064-7)
62. Park C, Nutt SR. Anisotropy and strain localization in steel foam. *Mater Sci Eng A.* 2001;299:68-74.
63. Li Y, Kang Z, Yan X, et al. A three-dimensional reticulate CNT-aerogel for a high mechanical flexibility fiber supercapacitor. *Nanoscale.* 2018;9:9360-9368. <https://doi.org/10.1039/c8nr01991f>
64. Kim KH, Oh Y, Islam MF. Graphene coating makes carbon nanotube aerogels superelastic and resistant to fatigue. *Nat Nanotechnol.* 2012;7(9):562-566. <https://doi.org/10.1038/nnano.2012.118>
65. Maestri CA, Abrami M, Hazan S, et al. Role of sonication pretreatment and cation valence in the sol-gel transition of nano-cellulose suspensions. *Sci Rep.* 2017;7(1):1-10. <https://doi.org/10.1038/s41598-017-11649-4>
66. Pan J, Ding D, Dong S, Liu Y, Wei N, Zhao J. A theoretical analysis of peeling behavior between nanowires and substrates in the ambient condition with high relative humidity. *Mech Mater.* 2017;114:243-253. <https://doi.org/10.1016/j.mechmat.2017.08.012>
67. Wadley HNG. Cellular metals manufacturing. *Adv Eng Mater.* 2002;4(10):726-733. [https://doi.org/10.1002/1527-2648\(20021014\)4:10<726::AID-ADEM726>3.0.CO;2-Y](https://doi.org/10.1002/1527-2648(20021014)4:10<726::AID-ADEM726>3.0.CO;2-Y)
68. Zhang B, Zhang J, Sang X, et al. Cellular graphene aerogel combines ultralow weight and high mechanical strength: a highly efficient reactor for catalytic hydrogenation. *Sci Rep.* 2016;6:1-10. <https://doi.org/10.1038/srep25830>
69. Roenbeck MR, Sandoz-Rosado EJ, Cline J, et al. Probing the internal structures of Kevlar® fibers and their impacts on mechanical performance. *Polymer (Guildf).* 2017;128:200-210. <https://doi.org/10.1016/j.polymer.2017.09.039>
70. Park B, Lee W, Lee E, Min SH, Kim BS. Highly tunable interfacial adhesion of glass fiber by hybrid multilayers of graphene oxide and aramid nanofiber. *ACS Appl Mater Interfaces.* 2015;7(5):3329-3334. <https://doi.org/10.1021/am5082364>
71. Buckingham DA, Keene FR, Sargeson AM. Base hydrolysis of coordinated acetonitrile. *J Am Chem Soc.* 1973;95(17):5649-5652. <https://doi.org/10.1021/ja00798a032>
72. Sun J, Hu Z, Li J, Zhang H, Sun C. Thermal and mechanical properties of fibrous zirconia ceramics with ultra-high porosity. *Ceram Int.* 2014;40:11787-11793. <https://doi.org/10.1016/j.ceramint.2014.04.008>
73. Zhang Q, Hao M, Xu X, Xiong G, Li H, Fisher TS. Flyweight 3D graphene scaffolds with microinterface barrier-derived tunable thermal insulation and flame retardancy. *ACS Appl Mater Interfaces.* 2017;9(16):14232-14241. <https://doi.org/10.1021/acsami.7b01697>
74. Wang J, Du R, Zhang X. Thermoresponsive polyrotaxane aerogels: converting molecular necklaces into tough porous monoliths. *ACS Appl Mater Interfaces.* 2018;10(2):1468-1473. <https://doi.org/10.1021/acsami.7b18741>

75. Wu S, Du A, Huang S, Sun W, Xiang Y, Zhou B. Solution-processable polyimide aerogels with high hydrophobicity. *Mater Lett.* 2016;176:118-121. <https://doi.org/10.1016/j.matlet.2016.04.099>
76. Leventis N, Chidambareswarapattar C, Mohite DP, Larimore ZJ, Lu H, Sotiriou-Leventis C. Multifunctional porous aramids (aerogels) by efficient reaction of carboxylic acids and isocyanates. *J Mater Chem.* 2011;21(32):11981-11986. <https://doi.org/10.1039/c1jm11472g>
77. Li J, Hu Z, Tan L, Jiang Z, Liu L, Huang Y. Preparation and properties of PIPD nanofibers made by a swelling and ultrasonic stripping process. *RSC Adv.* 2016;6(81):78073-78079. <https://doi.org/10.1039/c6ra09796k>
78. Kirpsza A, Lalik E, Mordarski G, Micek-Ilnicka A. Catalytic properties of carbon nanotubes-supported heteropolyacids in isopropanol conversion. *Appl Catal A Gen.* 2018;549:254-262. <https://doi.org/10.1016/j.apcata.2017.10.008>
79. Lakhi KS, Singh G, Kim S, et al. Mesoporous Cu-SBA-15 with Highly ordered porous structure and its excellent CO<sub>2</sub> adsorption capacity. *Microporous Mesoporous Mater.* 2018;267:134-141. <https://doi.org/10.1016/j.micromeso.2018.03.024>
80. Hrubesh LW, Pekala RW. Thermal properties of organic and inorganic aerogels. *J Mater Res.* 2007;9(03):731-738. <https://doi.org/10.1557/jmr.1994.0731>
81. Isobe T, Nishimura M, Matsushita S, Nakajima A. Gas separation using Knudsen and surface diffusion I: preparation of epoxy/porous SiO<sub>2</sub> composite. *Microporous Mesoporous Mater.* 2014;183:201-206. <https://doi.org/10.1016/j.micromeso.2013.09.028>
82. Wang L, Ma J, He X, Ke H, Liu J, Zhang C. Learning the deformation mechanism of poly(vinylidene fluoride-co-chlorotrifluoroethylene): an insight into strain-induced microstructure evolution via molecular dynamics. *J Mol Model.* 2017;23(12):361. <https://doi.org/10.1007/s00894-017-3529-z>
83. Yang M, Zhao N, Cui Y, et al. Biomimetic architected graphene aerogel with exceptional strength and resilience. *ACS Nano.* 2017;11(7):6817-6824. <https://doi.org/10.1021/acs.nano.7b01815>
84. Sai H, Fu R, Xing L, et al. Surface modification of bacterial cellulose aerogels' web-like skeleton for oil/water separation. *ACS Appl Mater Interfaces.* 2015;7(13):7373-7381. <https://doi.org/10.1021/acsami.5b00846>
85. Liao Q, Su X, Zhu W, et al. Flexible and durable cellulose aerogels for highly effective oil/water separation. *RSC Adv.* 2016;6(68):63773-63781. <https://doi.org/10.1039/c6ra12356b>
86. Gui X, Wei J, Wang K, et al. Carbon nanotube sponges. *Adv Mater.* 2010;22(5):617-621. <https://doi.org/10.1002/adma.200902986>
87. Zhang M, Gao B, Cao X, Yang L. Synthesis of a multifunctional graphene-carbon nanotube aerogel and its strong adsorption of lead from aqueous solution. *RSC Adv.* 2013;3(43):21099-21105. <https://doi.org/10.1039/c3ra44340j>
88. Hu H, Zhao Z, Wan W, Gogotsi Y, Qiu J. Polymer/graphene hybrid aerogel with high compressibility, conductivity, and "sticky" superhydrophobicity. *ACS Appl. Mater. Interfaces.* 2014;6(5):3242-3249. <https://doi.org/10.1021/am4050647>
89. Yin R, Cheng H, Hong C, Zhang X. Synthesis and characterization of novel phenolic resin/silicone hybrid aerogel composites with enhanced thermal, mechanical and ablative properties. *Compos Part A Appl Sci Manuf.* 2017;101:500-510. <https://doi.org/10.1016/j.compositesa.2017.07.012>
90. Arndt EM, Gawryla MD, Schiraldi DA. Elastic, low density epoxy/clay aerogel composites. *J Mater Chem.* 2007;17(33):3525-3529. <https://doi.org/10.1039/b704114d>
91. Xu M, Futaba DN, Yamada T, Yumura M, Hata K. Carbon nanotubes with temperature-invariant viscoelasticity from -196° to 1000°C. *Science.* 2010;330(6009):1364-1368. <https://doi.org/10.1126/science.1194865>
92. Xu M, Futaba DN, Yumura M, Hata K. Carbon Nanotubes with temperature-invariant creep and creep-recovery from -190 to 970°C. *Adv Mater.* 2011;23:3686-3691. <https://doi.org/10.1002/adma.201101412>
93. Sun F, Liu L, Kuang H, Xu C. Development of ELISA for melamine detection in milk powder. *Food Agric Immunol.* 2013;24(1):79-86. <https://doi.org/10.1080/09540105.2011.641170>
94. Kotal M, Kim H, Roy S, Oh I. Sulfur and nitrogen co-doped holey graphene aerogel for structurally resilient solid-state supercapacitors under high compressions. *J Mater Chem A.* 2017:17253-17256. <https://doi.org/10.1039/c7ta05237e>
95. Tang Y, Yeo L, Chen Y, Yap W, Cheng W. Ultralow-density copper nanowire aerogel monoliths with tunable mechanical and electrical properties. *J Mater Chem A.* 2013;1:6723-6726. <https://doi.org/10.1039/c3ta10969k>
96. Liao Q, Su X, Zhu W, Hua W, Qian Z. RSC advances flexible and durable cellulose aerogels for highly effective oil/water separation. *RSC Adv.* 2016;6:63773-63781. <https://doi.org/10.1039/C6RA12356B>
97. Nguyen ST, Feng J, Ng SK, Wong JPW, Tan VBC, Duong HM. Advanced thermal insulation and absorption properties of recycled cellulose aerogels. *Colloids Surfaces A Physicochem. Eng Asp.* 2014;445:128-134. <https://doi.org/10.1016/j.colsurfa.2014.01.015>
98. Sai H, Fu R, Xing L. Surface modification of bacterial cellulose aerogels' web-like skeleton for oil/water separation. *ACS Appl Mater Interfaces.* 2015;13:7373-7381. <https://doi.org/10.1021/acsami.5b00846>
99. Wang B, Zhang W, Zhang W, Mujumdar AS, Huang L. Progress in drying technology for nanomaterials. *Dry Technol.* 2005;23(1-2):7-32. <https://doi.org/10.1081/DRT-200047900>
100. Wu D, Fu R, Zhang S, Dresselhaus MS, Dresselhaus G. Preparation of low-density carbon aerogels by ambient pressure drying. *Carbon.* 2004;42(10):2033-2039. <https://doi.org/10.1016/j.carbon.2004.04.003>

**How to cite this article:** Li J, Li H, Xu L, et al. Biomimetic nanoporous aerogels from branched aramid nanofibers combining high heat insulation and compressive strength. *SmartMat.* 2021;e1019. <https://doi.org/10.1002/smm2.1019>